Mem. S.A.It. Vol. 86, 616

Memorie della

Modelling gas and dust in the Taurus and Perseus clouds with Fermi LAT and Planck data

Q. Remy, I. A. Grenier, D. J. Marshall, and J. M. Casandjian,
on behalf of Fermi LAT Collaboration

Laboratoire AIM, CEA-IRFU/CNRS/Université Paris Diderot, Service d'Astrophysique, CEA Saclay, 91191 Gif sur Yvette, France, e-mail: quentin.remy@cea.fr

Abstract. We have carried out a multi-wavelength study of the gas content in the different interstellar phases of the nearby Cetus, Taurus, Perseus, and California clouds. The gas tracers include HI and CO line data together with γ-ray observations with the Fermi Large Area Telescope (LAT) and observations of the thermal dust emission with Planck and IRAS. We have used them in order to (i) probe the gas tracers and cosmic-ray densities over a large range of hydrogen column densities and dust temperatures; (ii) map the dark neutral medium at the atomic-molecular interface; (iii) measure the CO-to-H_2 conversion factor, X_{CO}; and (iv) follow the evolution of the dust properties per gas nucleon as the gas becomes denser. The results show a uniform penetration of the cosmic rays to the dense CO-bright filaments, significant variations in grain opacity across the clouds as the gas densifies, X_{CO} values that tend to decrease from diffuse to compact clouds, and large quantities of dark neutral gas with a mass equivalent to that of the CO-bright phase.

1. Introduction

The study of the gas properties in the interstellar medium (ISM) of our Galaxy is based on a limited set of multi-wavelength tracers. Few of them, such as the 21 cm line emission of hydrogen (Kalberla et al. 2005, 2010; Peek et al. 2011) and the 2.6 mm line emission of ^{12}CO as a proxy for the molecular gas (Dame et al. 2001; Dame & Thaddeus 2004; Planck Collaboration 2014b), have been extensively observed across the sky. The large dust grains mixed with the gas are observable via their thermal emission in the sub-mm to infrared domains (Planck Collaboration 2014a). The interaction of high-energy cosmic rays (CRs) with nucleons of the interstellar gas provides a tracer of all chemical and thermodynamical forms of the gas to large depths into the clouds (Lebrun et al. 1982). These tracers are frequently used to quantify the gas column-densities even though our understanding of their limitations is still partial. Confronting them allows us to probe biases and to search for missing gas in the census.

In the continuity of the recent multi-tracer analysis of the Chamaeleon complex (Planck and Fermi Collaborations 2014), our goal is to test the dust and γ-ray tracing of the total gas against a linear combination of the emission line intensities recorded in HI and CO, plus the gas in the dark neutral medium (DNM) which escapes the radio surveys at the atomic-molecular interface because it combines optically thick HI and CO-dark or CO-faint molecular gas (van Dishoeck & Black 1988; Grenier et al. 2005). The Taurus region offers clouds with larger molecular mass and star-formation activity than the Chamaeleon region. In addition to the well-known Taurus molecular clouds (Ungerechts & Thaddeus 1987), the analysis region includes a nearby, diffuse and low-mass cloud which we name Cetus, as well as the active Perseus cloud, and the massive molecular complex associated with the California nebula. The analysed region spans a few hundred parsecs in the local ISM (see below).

In the following, we briefly present the data (Sect. 2) and the models built to describe the dust and γ-ray emissions (Sect. 3). We then discuss the results on the γ-ray spectrum (Sect. 4), on the X_{CO} factor (Sect. 5), on the different gas phases (Sect. 6), and on dust evolution (Sect. 7), before concluding.

2. Data

2.1. Gas data

The northern sky is not yet fully covered by high-resolution 21-cm line emission surveys, so for this analysis we have used a combination of the GALFA-HI (Peek et al. 2011) and the LAB (Kalberla et al. 2005) surveys. GALFA data-cubes were recovered from purcell.ssl.berkeley.edu and re-sampled into a 0°.125-spaced Cartesian grid. We used the narrow-band cubes with their original velocity resolution of 0.18 km/s LSR.

In order to trace the molecular gas we have used $^{12}CO_{1-0}$ observations at 115 GHz from the moment-masked CfA CO survey of the Galactic plane Dame et al. (2001); Dame & Thaddeus (2004). The data are sampled on a 0°.125-spaced Cartesian grid, except at low latitudes ($b < -50°$) where they have been over-sampled from 0°.25 to 0°.125. We have separated coherent entities in position (in Galactic coordinates), velocity, and distance. The details on the kinematic separation method are given in (Planck and Fermi Collaborations 2014). We have thus isolated seven main structures, named Cetus, Main Taurus, South Taurus, North Taurus, Perseus, California, and the background Galactic disc. They are depicted in CO in Fig. 1.

Distance estimates to the local clouds have been compiled from the photometric measurements of PanSTARRS-1 and the detection of reddening fronts toward stellar groups (Schlafly et al. 2014). We have delimited the clouds in our analysis region by their W_{CO} contour at 0.5 K km s^{-1} and we have selected the stars intercepting each (and only one) cloud in the list of Schlafly et al. (2014). The average distance of the reddening fronts to the stars toward Cetus, Main Taurus, South Taurus, North Taurus, Perseus, and California are 195±42 pc, 145±20 pc, 155±76 pc, 190±30 pc, 270±29 pc, and 410±24 pc, respectively.

The N_{HI} column-density and W_{CO} intensity maps of a specific component have been constructed by integrating the velocity profile of the lines with centroid falling in the right velocity interval for each (l,b) direction. This method accounts for the line spill-over from one velocity interval (i.e. cloud) to the next along crowded lines of sight. In order to account for the unknown HI optical depth, we have derived all the HI column-density maps for a sample of uniform spin temperatures (150, 200, 300, 400, 500, 600, 700, and 800 K) and for the optically thin case.

As Taurus is an active star forming region, there are significant quantities of warm ionized gas. In order to take into account its contribution, we have used the WMAP 9-year free-free map in the K band at 22 GHz (Bennett et al. 2013).

2.2. Dust data

In order to trace the dust column density, we have used the dust optical depth, τ_{353}, obtained at 353 GHz by modelling the spectral energy distributions (SED) of the large-grain thermal emission with modified black-body curves (Planck Collaboration 2014a). The temperature, T_{dust}, and spectral index of the SEDs were fitted to the Planck and IRAS data above 100 microns in each sky pixel. Hereafter, we also refer to the dust opacity as the optical depth per gas nucleon, τ_{353}/N_H.

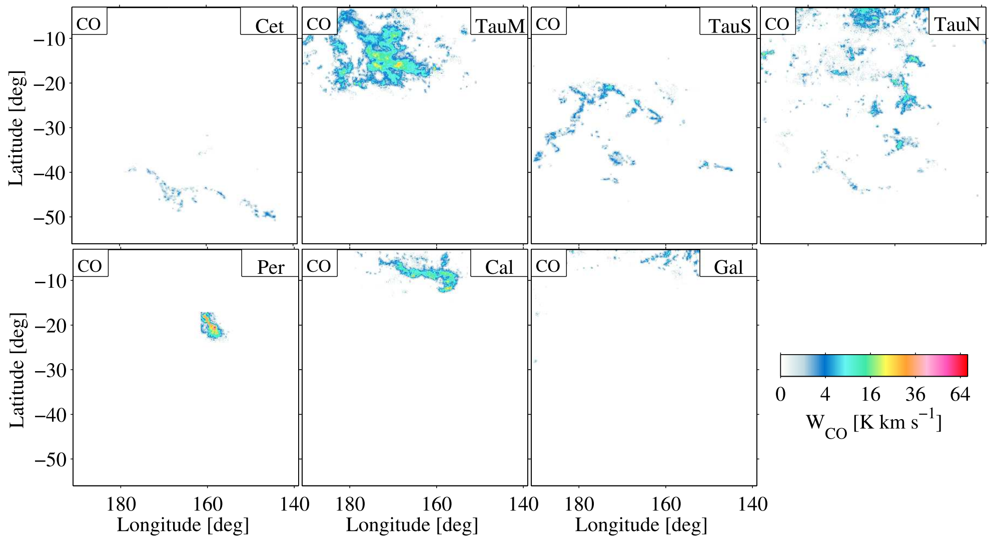

Fig. 1. Integrated CO intensity W_{CO}, in square-root scale, for the Cetus, Main Taurus, South Taurus, North Taurus, Perseus, and California clouds and the Galactic disc background.

2.3. γ-ray data

We have used the Pass 8 photon data from Fermi-LAT, its associated instrument response functions (IRFs, version P8v301), and the related isotropic spectrum for the extragalactic and residual instrumental backgrounds. We have calculated the IRFs, the exposure map, the γ-ray emissivity spectrum, q_{LIS}, of the local interstellar gas (Casandjian 2015), and the spectrum of the isotropic background in 14 energy bins, 0.2 dex in width and centred from $10^{2.3}$ to $10^{4.9}$ MeV. To ensure photon statistics robust enough to follow details in the spatial distributions of the different interstellar components, we have analysed the data in broad and independent energy bands, bounded by $10^{2.6}$, $10^{2.8}$, $10^{3.2}$, $10^{3.6}$, and 10^5 MeV. We have also analysed the data in the integrated $10^{2.6}$ - 10^5 MeV band. The low-energy threshold was set to take advantage of the best LAT point-spread-function (PSF) which strongly degrades at low energy. To optimize this PSF, we have selected all detected photons above 1.6 GeV, but only those at lower energy that converted to pairs in the front section of the tracker (Atwood et al. 2009).

To first order, the dust and γ-ray emissions should both trace the total gas column density, N_{H}. In order to compare them in Fig. 2, we have convolved the dust optical depth by the LAT response functions on the one hand, and we have subtracted non-gaseous γ-ray sources from the γ-ray data on the other hand. Fig. 2 shows strong similarities in the spatial distribution of both tracers, but it also reveals deviations in their dynamical range in several places.

3. Models

To detect gas unaccounted for in N_{HI} and W_{CO}, we have used the fact that it is permeated by both cosmic rays and dust grains. We have therefore extracted the significant γ-ray and dust residuals over the N_{HI}, W_{CO}, and N_{HII} expectations and we have used the spatial correlation between those residuals to infer the additional gas column densities. We have separated the residuals in two types of environments: in regions of weak or no CO intensity ($W_{\mathrm{CO}} < 7$ K km s^{-1}) which corresponds to the DNM at the atomic-molecular transition; and in regions toward CO intensities above this threshold to capture additional gas where ^{12}CO emission

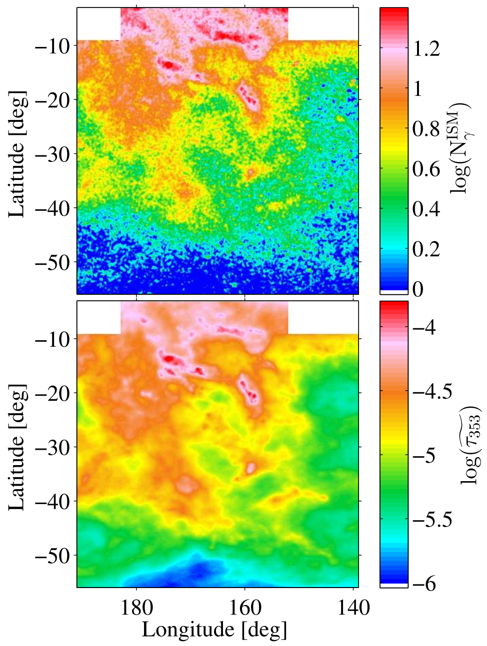

Fig. 2. Top : γ-ray count of gaseous origin in the $10^{2.6}$ - 10^5 MeV energy band. The map was constructed by subtracting the point sources and ancillary, non-gaseous, components from the data. Bottom : dust optical depth processed through the LAT IRFs.

saturates and rarer isotopologues such as ^{13}CO or $C^{18}O$ should be used.

3.1. Dust model

In the case of a uniform dust-to-gas mass ratio and uniform mass emission coefficient of the grains, the dust optical depth linearly scales with the total N_H. We have therefore modelled $\tau_{353}(l, b)$ in each direction as the linear combination of the gaseous contributions from the different phases (HII, HI, DNM, and CO-bright), with free normalisations to be fitted to the data, as in Planck and Fermi Collaborations (2014). We have added a free isotropic term to account for the residual noise and the uncertainty in the zero level of the dust data (Planck Collaboration 2014a).

3.2. γ-ray model

Earlier studies have indicated that the bulk of the Galactic CRs radiating in the energy bands selected for this work have diffusion lengths far exceeding typical cloud dimensions and that they efficiently diffuse through all the gas phases studied here. The observed γ-ray emission can thus be modelled, to first order, by a linear combination of the same gaseous components as in the dust model. We have assumed that the gas emissivity spectrum follows the average one found in the local ISM (q_{LIS}), but we have left a free normalisation in each energy band to account for possible deviations. The model also includes other radiation components such as the terrestrial limb emission, the Galactic inverse-Compton emission, point sources, and the isotropic flux mentioned above. In order to compare with the data, each component has been convolved in each energy band by the LAT response functions. We have used a binned maximum-likelihood with Poisson statistics to fit the modelled photon count map to the LAT data in each energy band (see Planck and Fermi Collaborations (2014) for further information).

4. γ-ray emissivity spectrum of the gas

The results of the analysis indicate that the emissivity spectra of the gas in the various phases of the different clouds are compatible with the average distribution in the local ISM (q_{LIS}). CR exclusion or concentration processes are strongly energy-dependent and we find no evidence for spectral variations in the γ-ray emission that would betray a concentration/exclusion effect in a particular cloud or with increasing gas density. As long as the CR spectrum is uniform in all the gas phases, the γ-ray map should remain a reliable tracer of the total gas.

We find small variations in absolute CR flux between the sampled clouds. This flux compares well with the local ISM average in Cetus and in the South and North Taurus clouds, but it exceeds the local average by 16±3%, 21±2%, and 36±8% respectively in the California, Main Taurus, and Perseus clouds. These variations apparently do not relate to the cloud altitude above the Galactic disc, which are estimated to be 64, 38 and 92 pc, respectively. They do not relate to the Galactocentric distance either. They are compatible with changes in HI spin temperature from cloud to cloud and inside clouds.

5. $X_{\rm CO}$ factors

5.1. γ-ray measurements

The $X_{\rm CO}$ factor is often applied to convert the $W_{\rm CO}$ intensity to the $N_{\rm H}$ column density in the molecular phase. It can be straighforwardly estimated in γ rays under the assumption of a uniform CR flux in the HI and CO-bright phases (Strong et al. 1988). In all the present clouds, we find $X_{\rm CO}$ values close to or lower than 10^{20} cm^{-2} K^{-1} km^{-1} s as in other local clouds analysed in γ rays where the values range from about 0.6 to 1.1 in unit of 10^{20} cm^{-2} K^{-1} km^{-1} s (Abdo et al. 2010; Ackermann et al. 2012b,a; Planck and Fermi Collaborations 2014). We find a low factor of $(0.49 \pm 0.05)\times10^{20}$ cm^{-2} K^{-1} km^{-1} s in Perseus, but it may be biased by some degeneracy between the $N_{\rm HI}$ and $W_{\rm CO}$ maps of this compact cloud, after convolution with the LAT PSF. If we force the γ-ray emissivity of the HI gas to be the same as in the remote California cloud, we obtain a larger $X_{\rm CO}$ value of $(0.66 \pm 0.04)\times10^{20}$ cm^{-2} K^{-1} km^{-1} s, but the fit quality is significantly poorer, by $3.9\,\sigma$. The low $X_{\rm CO}$ value we find in γ rays at the scale of 1–2 pc supports the low average of 0.3×10^{20} cm^{-2} K^{-1} km^{-1} s found at higher resolution from the dust, HI, and CO study of Lee et al. (2014).

Figure 3 compares $X_{\rm CO}$ measurements obtained in γ rays with the same method in nearby clouds (from Planck and Fermi Collaborations (2014) and this work). We find that the average $X_{\rm CO}$ factor in a cloud does not depend on the H_2 mass mapped in CO, but it depends on the cloud structure, in particular on its diffuseness. Changes in the latter are reflected in the average value, $\overline{W_{\rm CO}}$, of the $W_{\rm CO}$ intensities over a cloud, or in the surface fraction of dense regions with large $W_{\rm CO}$ intensity within a cloud:

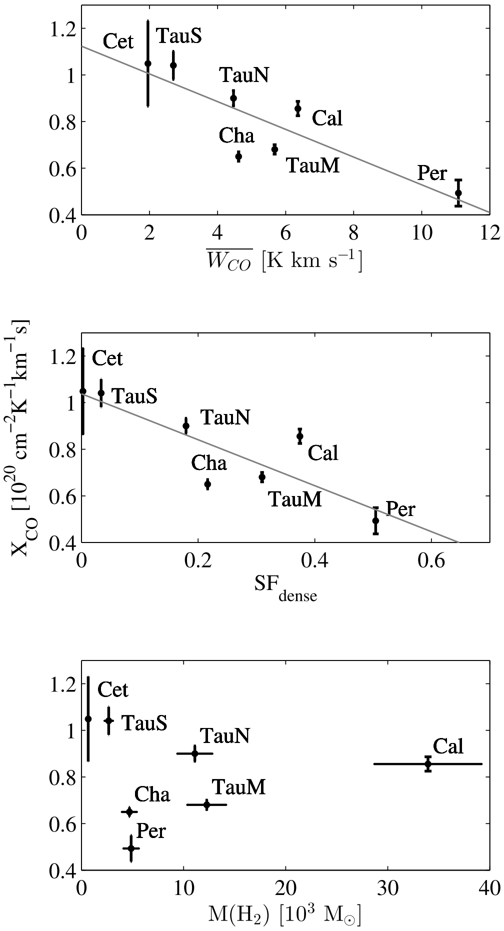

Fig. 3. Evolution of the $X_{\rm CO}$ factor in the different clouds as measured in γ rays in the total energy band. The evolution is displayed with the average CO intensity, $\overline{W_{\rm CO}}$, measured in a cloud above 1 K km s^{-1} *(top)*, with the surface fraction, SF$_{\rm dense}$, of the dense cores (see Eq. 1) *(middle)*, and with the H_2 mass found in the CO-bright phase of the clouds *(bottom)*. The Chamaeleon data comes from Planck and Fermi Collaborations (2014).

$$\mathrm{SF}_{\rm dense} = \frac{\mathrm{S}_{W_{\rm CO}>7\ \mathrm{K\,km/s}}}{\mathrm{S}_{W_{\rm CO}>1\ \mathrm{K\,km/s}}} \quad (1)$$

Figure 3 shows that $X_{\rm CO}$ tends to decrease from diffuse to more compact clouds. This trend remains if we use the Perseus value found when

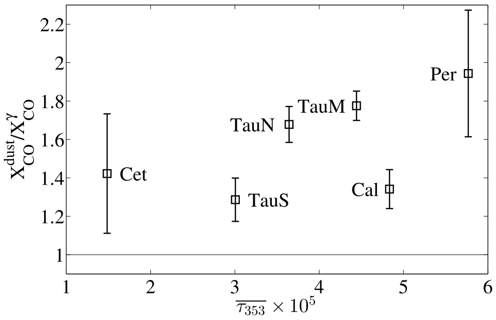

Fig. 4. Evolution of the ratio between the dust and γ-ray measurements of X_{CO} in the different clouds as a function of the average dust optical depth, $\overline{\tau_{353}}$, in the cloud.

forcing the Hɪ γ-ray emissivity or if we exclude the Perseus data point. The trend is consistent with the expectation that X_{CO} decreases from the diffuse envelopes, exposed to the interstellar radiation field, to the shielded cores of the CO clouds (Sheffer et al. 2008; Liszt & Pety 2012; Bolatto et al. 2013; Lee et al. 2014). According to X_{CO} calculations as a function of visual extinction A_V (Bell et al. 2006), X_{CO} drops by an order of magnitude with increasing A_V, down to a minimum at $1 \lesssim A_V \lesssim 2$ mag. The minimum value reaches below 10^{20} cm^{-2} K^{-1} km^{-1} s for hydrogen densities larger than 10^3 cm^{-3} and it depends on the cloud age and turbulence level. So, we expect the average X_{CO} over a cloud to vary with the relative solid angle subtended by the diffuse and dense parts of the clouds.

5.2. Dust measurements

The results of the dust model provide an independent measure of X_{CO}. Figure 4 shows that the dust-derived X_{CO} factors are systematically 30% to 100% higher than the γ-ray values. Such discrepancies had already been noted in previous studies (Dame et al. 2001; Grenier et al. 2005; Planck Collaboration 2011a; Bolatto et al. 2013), but on the basis of different Hɪ and CO surveys, different correlation methods, and different angular resolutions. In the present study, the dust and γ-ray models are fitted to the same N_{HI} and W_{CO} maps, at the same resolution. It has been proposed that the inclusion of the DNM gas in γ-ray analyses and not in dust analyses could explain the lower X_{CO} values obtained in γ rays (Bolatto et al. 2013). It is argued by Planck and Fermi Collaborations (2014) that, by construction, the inclusion of the DNM map cannot bias the X_{CO} estimate. Furthermore, the recent analyses include the DNM in both the dust and γ-ray fits and we have verified in this work that the X_{CO} factor derived in γ rays changes only by about 10% when the DNM phase is added or not to the fits. A change in dust emission properties can bias the X_{CO} factor upward. We show in Sect. 7 evidence for departure from linearity of the dust opacity, τ_{353}/N_H, in dense CO regions. This rise is perceptible in Figure 4.

6. Gas phases in the clouds

Figure 5 presents the N_H column-density maps derived in the Hɪ, DNM, and CO phases. The latter is based on the W_{CO} maps and X_{CO} ratios of the individual cloud complexes. The structure in the DNM map comes from the dust data, but it is scaled in mass with the γ-ray emission under the assumption of a uniform CR flux between the Hɪ and DNM phases. This assumption is substantiated by the uniform CR spectrum found in the Hɪ, DNM, and CO phases. The DNM structures often surround the denser CO-bright parts of the clouds. This is well illustrated around the faint CO clumps of Cetus and South Taurus. The DNM represents about 15% of the total mass in the analysed region. It slightly exceeds the mass in the CO-bright phase.

Dense DNM clumps reaching 10^{22} cm^{-2} have been found toward bright CO cores of the Chamaeleon complex (Planck and Fermi Collaborations 2014). They could plausibly relate to the saturation of the W_{CO} intensities because of the large optical thickness of the dense molecular gas to ^{12}CO ($J = 1 \to 0$) line emission. We have used the dust and γ-ray data in regions where $W_{CO} > 7$ K km s^{-1} in order to map the gas column density in excess of that linearly traced by W_{CO}. Figure 6 presents a zoom of this map on the Taurus

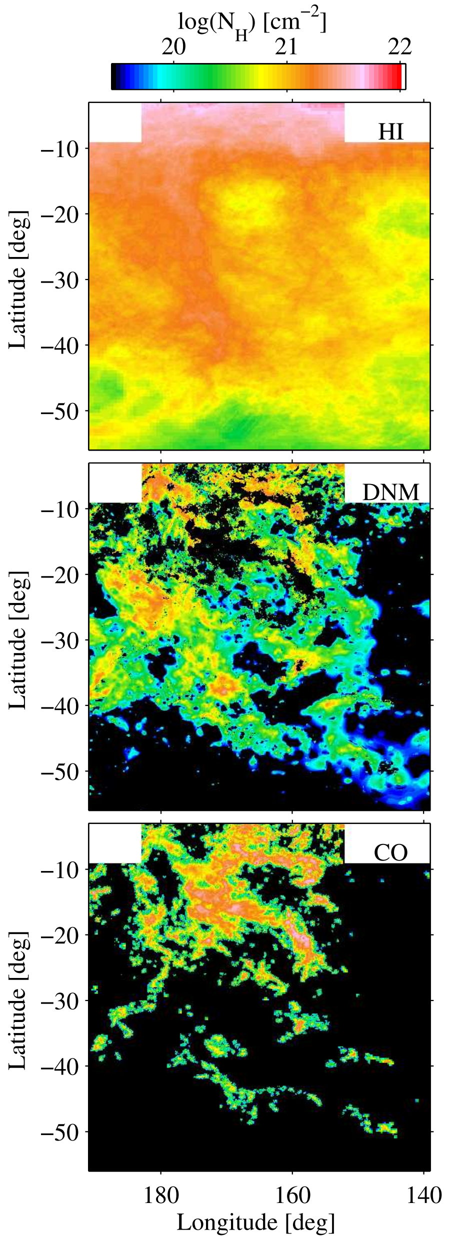

Fig. 5. Hydrogen column density maps, N_{H}, in the HI, DNM, and CO-bright phases, obtained for an HI spin temperature of 400 K. The N_{H} map in the DNM is based on the dust residuals over the HII, HI, and CO expectations and on the average the $\tau_{353}/N_{\mathrm{H}}$ opacity measured in γ rays in this phase. The N_{H} map in the CO phase uses the X_{CO} factors measured in γ rays for each cloud.

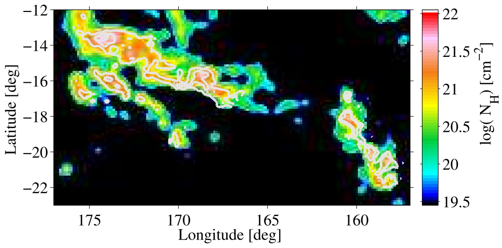

Fig. 6. Hydrogen column density map, N_{H}, of additional gas obtained in the ^{12}CO-saturated part of the Taurus and Perseus clouds, and overlaid with the ^{13}CO contours at 2 and 4 K km s^{-1} from Narayanan et al. (2008); Ridge et al. (2006).

and Perseus clouds. At large column densities, the detected filaments tightly follow the structure of the dense gas delineated with the integrated ^{13}CO line intensity (Narayanan et al. 2008; Ridge et al. 2006). The quantative comparison and degree of correlation between the N_{H} map and $W(^{13}\mathrm{CO})$ intensity is being studied. The additional gas represents about 20% of the ^{12}CO-bright mass in the analysis region. The spectrum of the γ-ray emission associated with this component is consistent with that of the other gas phases over the 0.4-100 GeV energy range. This implies a gaseous origin of the γ-ray emission, but also that the CRs can diffuse through the denser parts of the clouds, optically thick to ^{12}CO line emission.

7. Dust evolution

In order to follow changes in dust opacity, $\tau_{353}/N_{\mathrm{H}}$, we have built two maps of the total N_{H} column density in the region. The first one, $N_{\mathrm{H}\,\gamma}$, takes advantage of the CR interactions with gas in all chemical forms and thermodynamical states. The γ-ray intensity from the ISM has been obtained from the LAT data in the overall energy band after subtraction of the γ-ray counts unrelated to gas in the best-fit model. We have converted this γ-ray intensity into N_{H} using the emission rate found in the local atomic gas. The second map, $N_{\mathrm{H\,m}\lambda}$, uses the higher resolution information from the HI, CO, and dust data, and the mass scaling provided by the best-fit γ-ray model (uniform HI spin temperature, X_{CO} factors in the clouds, average $\tau_{353}/N_{\rm H}$ in the DNM, and γ-ray emissivity in the ionized gas). We note, however, that the opacity distribution at the smallest angular scales is less reliable because the scaling factors used to construct $N_{\rm H\,m\lambda}$ have been derived at the scale of a whole cloud.

Fig. 7 shows the 2D histogram of the correlation between the sighline integrals of the dust optical depth and $N_{\rm H\gamma}$ column density. It exhibits a departure from linearity in dust opacity with increasing $N_{\rm H}$ above a few 10^{21} cm^{-2}. Opacity maps (not shown here) indicate that $\tau_{353}/N_{\rm H}$ progressively evolves within the clouds, especially in the dense CO filaments, but also through the more diffuse DNM. They corroborate, thanks to the total gas tracing capability of the CRs, earlier indications of dust evolution in the Taurus CO filaments based on IRAS, Spitzer, Planck, and Hershel observations (Stepnik et al. 2003; Flagey et al. 2009; Planck Collaboration 2011b; Ysard et al. 2013).

Other molecular clouds present an opacity rise in dense regions suggesting grain evolution as they coagulate to form fluffy aggregates and/or as they get covered by ice mantles (Martin et al. 2012; Roy et al. 2013; Planck and Fermi Collaborations 2014). In order to determine how these variations depend on the ambient ISM, Fig. 8 shows how the opacity varies with the molecular fraction in the gas column, f_{H_2}, with the total $N_{\rm H\,m\lambda}$ column density as traced by the multi-wavelength data, and with the dust colour temperature. We detect a strong rise by a factor of three in the cold, molecular gas enviromnent. As in the Chamaeleon clouds (Planck and Fermi Collaborations 2014), the increase in $\tau_{353}/N_{\rm H}$ does not relate to an increase in the specific power radiated by the grains because of a local enhancement in heating rate, near young stars for instance. On the contrary, we have measured that the specific power decreases by a factor of up to 2 in the shaded CO regions of all the analysed clouds.

The conditions of the cold molecular phase are not the only possible cause for dust evolution. In the atomic gas, we obtain a mean opacity in the Cetus, Taurus, and California clouds 30% to 100% larger than the average of $(7.1 \pm 0.6)\times 10^{-27}$ cm^2 H^{-1} measured in the high-

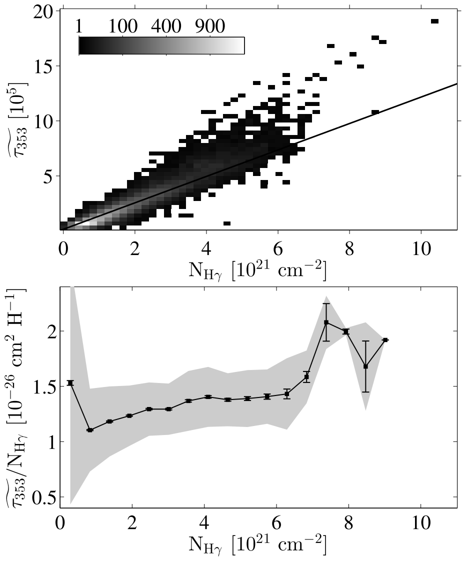

Fig. 7. *Top:* 2D histograms of the correlations between the total gas column density, $N_{\rm H\gamma}$, measured with the 0.4-100 GeV interstellar γ rays, and the dust optical depth convolved with the LAT response. *Bottom:* evolution of the dust opacity in equally spaced bins in $N_{\rm H\gamma}$. The error bars and shaded areas give the standard error on the mean and standard deviation in each bin.

latitude cirruses (Planck Collaboration 2014c). So, we confirm the observation of large opacity variations within the atomic phase at column densities below 10^{21} cm^{-2}. This change within the diffuse atomic phase challenges current dust evolution models.

8. Conclusion

We have analyzed the gas, dust and CR content of several clouds in the Taurus, Perseus, and Cetus regions. The γ-ray emissivity of the gas in these clouds has the same energy spectrum as in other clouds of the local ISM. In the 0.4–100 GeV energy band and at the precision level of the current LAT observations, we find no evidence of CR exclusion or CR concentration in the clouds, up to the dense filaments traced in ^{13}CO.

The DNM represents 10% to 20% of the total mass of a given cloud in this sample. When integrated over the whole analysis region, the

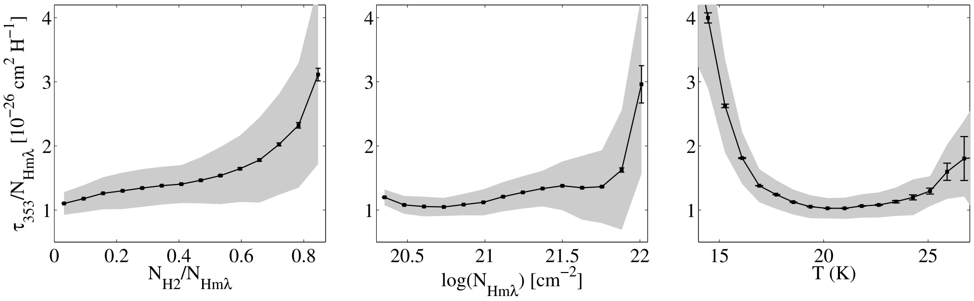

Fig. 8. Evolution of the dust opacity as a function of the molecular fraction in the gas column *(left)*, the total gas column density $N_{\mathrm{H\,m}\lambda}$ *(middle)*, and the dust color temperature *(right)*. To estimate the molecular fraction in N_H, the DNM is assumed to be 50% molecular. The error bars and shaded areas give the standard error on the mean and standard deviation in each bin.

DNM is slightly more massive than the molecular gas observed in CO. The DNM dominates the molecular phase up to a visual extinction of about 1 magnitude if it is more than half molecular.

The dust and γ-ray data indicate that the gas column density continues to increase when the ^{12}CO line intensity saturates. The structure of the additional gas follows that of the optically-thinner ^{13}CO line intensity. The added gas dominates the molecular phase at $A_\mathrm{V} \gtrsim 5$ magnitudes.

The dust opacity at 353 GHz, τ_{353}/N_H, appears to rise by a factor three from low column densities in the atomic gas (about 10^{-26} cm^2 H^{-1}) to cold grains in molecular gas at $N_\mathrm{H} \gtrsim 5 \times 10^{21}$ cm^{-2}. The amplitude of the rise compares with the variations observed in the Chamaeleon clouds (Planck and Fermi Collaborations 2014). As the observed specific power radiated by the grains decreases in the cold molecular region, the changes cannot be attributed to a larger heating rate, but they are more likely caused by a chemical or structural evolution of the grains. The magnitude of the rise severely limits the use of the thermal emission of the big grains to trace the total gas. The linear regime is limited to $N_\mathrm{H} < 3\times10^{21}$ cm^{-2} in these clouds. The confirmation of large opacity variations across clouds directly impacts the gas mass estimates inferred from dust emission at sub-mm and mm wavelengths to derive star-forming efficiencies in the Galaxy and in external galaxies. We will further confront the gas, γ-ray, and dust data in the nearby clouds using dust column densities inferred from stellar reddening and absorption data.

We provide independent measurements of the X_CO factor from the dust and γ-ray analyses in six different clouds, against the same HI and CO data. As in the Chamaeleon complex, we find that the dust-derived values are systematically larger, by 30% to 100% , than the γ-ray estimates. The difference is likely due to dust evolution with increasing N_H. The X_CO factors measured in γ rays range from $(1.05 \pm 0.18)\times 10^{20}$ cm^{-2} K^{-1} km^{-1} s in Cetus to $(0.49 \pm 0.056)\times 10^{20}$ cm^{-2} K^{-1} km^{-1} s in Perseus. They appear to decrease with the average W_CO intensity of the cloud and with the surface fraction subtended by the bright CO clumps inside the cloud: the more diffuse CO clouds tend to have larger average X_CO factors. Models of the formation and photodissociation of H_2 and CO molecules predict that X_CO should decrease from the diffuse envelopes of clouds to their dense cores (e. g. Bell et al. 2006). We will further investigate if the trends shown in Fig. 3 are consistent with theoretical predictions.

Acknowledgements. The *Fermi*-LAT Collaboration acknowledges support for LAT development, operation and data analysis from NASA and DOE (United States), CEA/Irfu and IN2P3/CNRS (France), ASI and INFN (Italy), MEXT, KEK, and JAXA (Japan), and the K.A. Wallenberg Foundation, the Swedish Research Council and the National Space Board

(Sweden). Science analysis support in the operations phase from INAF (Italy) and CNES (France) is also gratefully acknowledged.

The French authors acknowledge the support of the Agence Nationale de la Recherche (ANR) under award number STILISM ANR-12-BS05-0016.

References

Abdo, A. A., Ackermann, M., Ajello, M., et al. 2010, ApJ, 710, 133
Ackermann, M., Ajello, M., Allafort, A., et al. 2012a, ApJ, 756, 4
Ackermann, M., Ajello, M., Allafort, A., et al. 2012b, ApJ, 755, 22
Atwood, W. B., Abdo, A. A., Ackermann, M., et al. 2009, ApJ, 697, 1071
Bell, T. A., et al. 2006, MNRAS, 371, 1865
Bennett, C. L., Larson, D., Weiland, J. L., et al. 2013, ApJS, 208, 20
Bolatto, A. D., Wolfire, M., & Leroy, A. K. 2013, ARA&A, 51, 207
Casandjian, J.-M. 2015, ApJ, 806, 240
Dame, T. M., Hartmann, D., & Thaddeus, P. 2001, ApJ, 547, 792
Dame, T. M. & Thaddeus, P. 2004, in Milky Way Surveys: The Structure and Evolution of our Galaxy, eds. D. Clemens, R. Shah, & T. Brainerd (ASP, San Francisco), ASP Conf. Ser., 317, 66
Flagey, N., Noriega-Crespo, A., Boulanger, F., et al. 2009, ApJ, 701, 1450
Grenier, I. A., Casandjian, J.-M., & Terrier, R. 2005, Science, 307, 1292
Kalberla, P. M. W., Burton, W. B., Hartmann, D., et al. 2005, A&A, 440, 775
Kalberla, P. M. W., McClure-Griffiths, N. M., Pisano, D. J., et al. 2010, A&A, 521, A17
Lebrun, F., Paul, J. A., Bignami, G. F., et al. 1982, A&A, 107, 390
Lee, M.-Y., Stanimirović, S., Wolfire, M. G., et al. 2014, ApJ, 784, 80
Liszt, H. S. & Pety, J. 2012, A&A, 541, A58
Martin, P. G., Roy, A., Bontemps, S., et al. 2012, ApJ, 751, 28
Narayanan, G., Heyer, M. H., Brunt, C., et al. 2008, ApJS, 177, 341
Peek, J. E. G., Heiles, C., Douglas, K. A., et al. 2011, ApJS, 194, 20
Planck and Fermi Collaborations. 2014, ArXiv e-prints, 1409.3268
Planck Collaboration. 2011a, A&A, 536, A19
Planck Collaboration. 2011b, A&A, 536, A25
Planck Collaboration. 2014a, A&A, 571, A11
Planck Collaboration. 2014b, A&A, 571, A13
Planck Collaboration. 2014c, A&A, 566, A55
Ridge, N. A., Di Francesco, J., Kirk, H., et al. 2006, AJ, 131, 2921
Roy, A., Martin, P. G., Polychroni, D., et al. 2013, ApJ, 763, 55
Schlafly, E. F., Green, G., Finkbeiner, D. P., et al. 2014, ApJ, 786, 29
Sheffer, Y., Rogers, M., Federman, S. R., et al. 2008, ApJ, 687, 1075
Stepnik, B., Abergel, A., Bernard, J.-P., et al. 2003, A&A, 398, 551
Strong, A. W., Bloemen, J. B. G. M., Dame, T. M., et al. 1988, A&A, 207, 1
Ungerechts, H. & Thaddeus, P. 1987, ApJS, 63, 645
van Dishoeck, E. F. & Black, J. H. 1988, ApJ, 334, 771
Ysard, N., Abergel, A., Ristorcelli, I., et al. 2013, A&A, 559, A133